CrossMark
← click for updates

Self-assembled Ni/NiO/RGO heterostructures for high-performance supercapacitors

Yachao Zhu,[a] Wei Chu,*[a] Ning Wang,[c] Tao Lin,[a] Wen Yang,[a] Jie Wen*[b] and X. S. Zhao[d]

A nano-sized nickel/nickel oxide/RGO (Ni/NiO/RGO) nano-hybrid was generated successfully by using a facile and green sol–gel approach, with the reduced graphene oxide as an effective component, for developing a high-efficiency electrode material with super-capacitance. In the novel hierarchical nano-composite, the combination of metallic nickel interfaced with the nickel oxide was created by the reduction of a nickel nitrate precursor with the carbon of the reduced graphene oxide surface, during the thermal treatment in nitrogen. The electrochemical performances of the Ni/NiO/RGO composite were measured through cyclic voltammetry tests and galvanostatic charge–discharges, as a supercapacitor material. Due to the higher conductivity and synergistic effect, the new hybrid delivered a high specific capacitance of 1027.27 F g^{-1} at the charge/discharge current density of 2 A g^{-1}, and 720 F g^{-1} at 20 A g^{-1}. After 1000 uninterrupted cycles at 5 A g^{-1}, the high specific capacitance value can be still stabilized, and kept at 92.95% of the initial value of the specific capacitance for Ni/NiO/RGO. This new nano composite with RGO and Ni/NiO exhibits great promise as an electrode material for supercapacitors.

Introduction

Over recent years, with a fast-growing market for developing new, low-cost and environmentally friendly energy storage devices, there has been an ever-increasing and urgent demand for high-power energy resources. (Now-a-days, it is essential that clean and highly efficient energy storage devices be found, in response to the ever-increasing energy demands and concerns about environmental issues.)[1–9] Supercapacitors (also called electro-chemical capacitors and ultracapacitors), as promising energy storage devices, have attracted a great deal of attention because of their high power performance, long cycle life and high dynamics of charge propagation.[10–17] Based on the energy storage mechanism,[18] supercapacitors can be divided into two kinds: electric double-layer capacitors (EDLCs) and pseudoca-pacitors.[19–21] The energy storage capacity in EDLCs is built on the charge adsorption of electrolyte ions on the surface of the electrodes.[22] In contrast, the charge storage of the pseudoca-pacitors arises from fast and reversible faradaic processes, which involve surface or near-surface redox reactions.[23,24] Generally, the specific capacitance value of pseudocapacitors is significantly higher than those of EDLCs capacitors.[25–27] Since the performance of pseudo-capacitors is largely determined by or depends upon the electrode materials, the progress of high-capacitor supercapacitor research concentrates on the devel-opment of electrode materials.[13,28,29]

Graphene,[30] with a two dimensional hexagonal lattice of sp^2 carbon atoms covalent structure, has recently been found to be an ideal substrate for growing and anchoring of electrode materials to improve the electrochemical performance of elec-trode, due to extraordinary electrical conductivity, thermal properties and high specific surface areas.[31–35] Then, graphene-based electrode materials for supercapacitors are reviewed.[36] Nevertheless, the capacitances are mainly limited by the restacking and agglomeration of graphene sheets, which will lead to great loss of effective area and exhibit lower capacitances than as expected and thus hamper the performance of super-capacitors using graphene materials.[37–39]

Then again, transition metal oxides have been widely used as pseudocapacitive electrode materials.[40–43] Transition-metal oxides can produce larger capacitance owing to multielectron transfer during fast faradaic reactions and their multiple oxide states.[44,45] Among the metal oxides, RuO_2 has attracted great interest because of its superior electrochemical performance such as high specific capacitance, wide potential windows and high electrochemical stability. However, the high cost of the raw materials impedes its commercialization.[46] As a promising candidate, the nickel oxide (NiO)[47] has displayed outstanding properties due to low price and high capacitance.[48,49] But the specific capacitance of NiO is much lower than its theoretical

[a]Department of Chemical Engineering, Sichuan University, Chengdu 610065, China. E-mail: chuwei1965@scu.edu.cn

[b]College of Chemistry and Chemical Engineering, Southwest Petroleum University, Chengdu 610065, China

[c]Beijing Key Laboratory of Green Chemical Reaction Engineering and Technology, Department of Chemical Engineering, Tsinghua University, Beijing 100084, China

[d]Department of Chemical Engineering, University of Queensland, Brisbane 4067, Australia. E-mail: george.zhao@uq.edu.au

value (2583 F g^{-1} within 0.5 V), resulting from relatively poor electrical conductivity and low accessible surface areas.[50–52] Yet, one effective solution to this problem is to develop the transition-metal oxides coupled with the reduced graphene oxide, which cannot only decrease the possibility of serious restacking and agglomeration of graphene substrate, but also combine the advantages of both materials, resulting in a great electrochemical performance.

Recent works have shown NiO coupled with reduced graphene for supercapacitor applications. Cao et al.[53] fabricated NiO/reduced graphene oxide by a facile hydrothermal route. The NiO particles with mesoporous structure were randomly anchored onto the surface of graphene sheets. Due to the 3D graphene conductive network and the mesoporous structure, the composite exhibited a very high specific capacitance of 800.4 F g^{-1}. Huang et al.[46] designed a 3D hierarchically porous NiO–graphene. First, multilayered porous graphene sheet network was constructed via a so-called "on-water spreading" method. And then, the cross-like NiO nanoflakes film were uniformly grown onto the graphene sheet framework by a chemical bath deposition. The hybrid exhibited specific capacitance of 540 F g^{-1} at 2 A g^{-1}. Zhu et al.[54] prepared the reduced graphene oxide–nickel oxide composite by homogeneous coprecipitation and subsequent annealing. It was found that NiO particles had a nanosheet-based microsphere structure and anchored uniformly on the surface of reduced graphene oxide platelets. The composite-based supercapacitor displayed high specific capacitance of 770 F g^{-1}. Singh et al.[55] fabricated a novel 1D core/shell Ni/NiO nano-architecture electrodes as a pseudocapacitor by hydrogenation. The nanohetero-composite had a high specific capacitance of 717 F g^{-1} at a scan rate of 2 mV s^{-1}.

In this work, the hierarchical novel Ni/NiO/RGO nanocomposite was synthesized by a sol–gel method combined with subsequent in situ annealing. As electrode materials for electrochemical supercapacitors, the hybrid shows a high specific capacitance and good cycling stability, which suggests their potential application in supercapacitors.

Experimental

Materials preparation

Graphite oxide (GO) was prepared from natural graphite by a modification of the Hummers method.[56]

The Ni/NiO/RGO hybrid was synthesized by a sol–gel method combined with subsequent in situ annealing. The typical preparation process is illustrated as follows. First, 0.207 g of graphene oxide (GO) was uniformly dispersed in 40 mL of deionized water by ultrasonication for 2 h, then, 4.144 g of Ni(NO$_3$)$_2$·6H$_2$O and 0.856 g of H$_2$C$_2$O$_4$ were dissolved in the above solution by ultrasonication for 30 min. The resulting solution was then stirred at 70 °C to promote gelation. The as-prepared product was dried at 80 °C in vacuum for 48 h, and then annealed at 400 °C for 2 h under an atmosphere of nitrogen in order to obtain a Ni/NiO/RGO hybrid. For comparison, the pristine NiO and RGO were also synthesized by the same procedure.

Characterization

The microstructure and surface morphology of Ni/NiO/RGO hybrid and NiO were characterized by transmission electron microscopy (TEM, JEOL, JEM-2010, Japan) and scanning electron microscopy (SEM, Hitachi, S3400, Japan). The crystallite structure was analyzed by X-ray diffraction (XRD, DX-2700, China) using Cu Kα radiation. IR spectra were obtained on a Fourier transform infrared (FT-IR, Bruker Tensor, Germany) spectrometer in the range from 400 to 4000 cm^{-1}. The specific surface area were investigated by nitrogen adsorption/desorption experiments (Quadrasorb SI).

Electrochemical characterization

The electrochemical performance measurements were studied in a three electrode electrochemical system containing 6 M KOH aqueous solution as the electrolyte, with an Hg/HgO electrode as the reference electrode and graphite electrode as the counter electrode. Cyclic voltammetry (CV), chronopotentiometry and electrochemical impedance spectroscopy (EIS) were measured on a CHI660e electrochemical workstation (Chenhua, Shanghai, China). The working electrode was prepared directly using the as-prepared products, acetylene black and polyvinylidene fluoride (PVDF) at a weight ratio of 8 : 1 : 1, which was then coated on clean Ni foam (1 cm × 1 cm) and dried at 80 °C for 12 h. Then the working electrodes were obtained by pressing the active material coated Ni foam under 10 MPa pressure. Thus, the loading density of the electrode active material was around 3 mg cm^{-2}.

Results and discussion

The XRD patterns of NiO, Ni/NiO/RGO hybrid, GO and RGO samples are shown in Fig. 1. For GO, there is a dominant peak
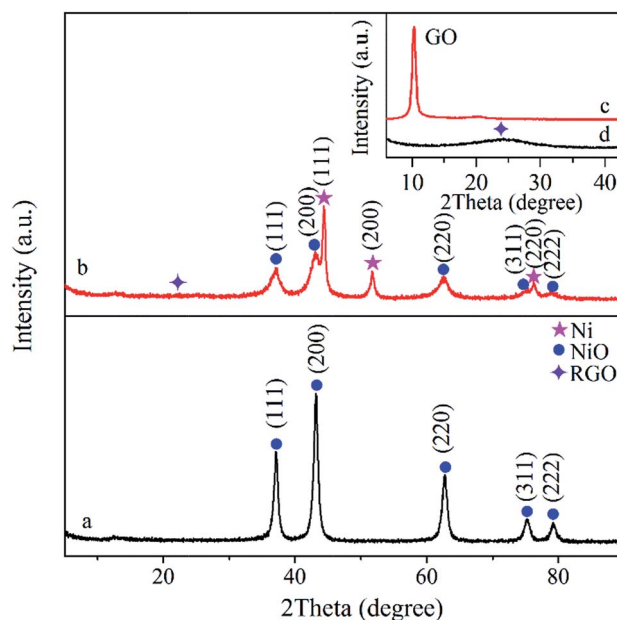

Fig. 1 XRD patterns of (a) NiO, (b) Ni/NiO/RGO, (c) GO and (d) RGO.

centered at $2\theta = 10.4$, corresponding to the (002) reflections of GO. However, after thermo-treatment, this band disappeared and meanwhile a broad peak centered at around $2\theta = 23$ in Fig. 1(d), indexed into the RGO sheets, emerged, suggesting the conversion of GO into RGO. For pure NiO, the sharp diffraction peaks in Fig. 1(a) can be indexed as (111), (200), (220), (311) and (222) crystal planes of the face-centered-cubic NiO phase (JCPDS no. 65-2901). In contrast, the hybrid in Fig. 1(b) not only has the characteristic peaks of NiO (space group Rm) rock salt, but it has the characteristic peaks of Ni, which reveals the partial reduction of nickel nitrate precursor by the carbon of the reduced graphene oxide surface during the thermos-treatment. Besides, there arises a small and broad diffraction peak at $2\theta = 23$, which can be indexed into the stacked RGO sheets. Then again, the peak is very weak, which maybe result from a more disordered stacking and quite uniform dispersion of the graphene sheets in the hybrid. Noticeably, when assembling NiO onto the graphene substrate, the NiO' crystal structure was significantly altered. The NiO-assigned diffraction lines are considerably attenuated, suggesting that NiO nanoparticles in the composite have the smaller crystalline size and higher dispersion. The XRD pattern can reveal a significant line broadening, which is a feature of nanoparticles. Thus, we can calculate the crystallite size by the well-known Debye–Scherrer formula.[57] And, the calculated NiO particle size is 5 nm for the composite and 11 nm for bare NiO. Obviously, this dramatic downsizing effect can be conferred on by the graphene substrate. Meanwhile, three new diffraction peaks at 44.52°, 51.75°, and 76.29° indexed to the (111), (200), and (220) Ni planes in Fig. 1(b), respectively, were also observed, indicating that during our synthetic procedures the obvious phase transition of NiO into metallic Ni occurred. This result indicates that the products are actually a hybrid of the small-sized metallic nickel and nickel oxide formed on the reduced graphene oxide (Ni/NiO/RGO).

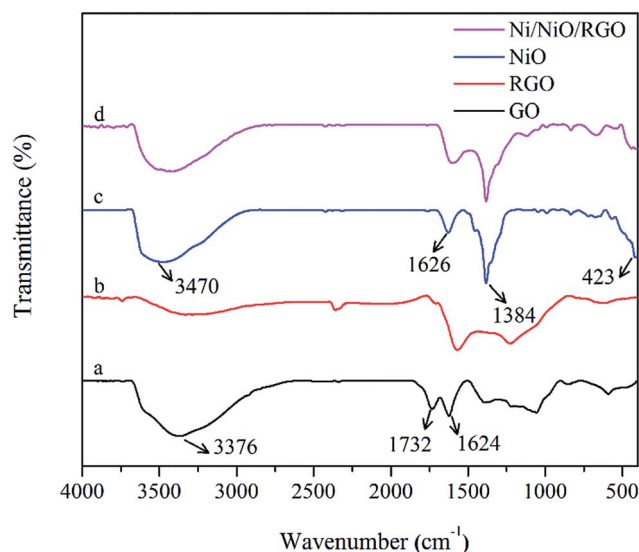Fig. 2 shows the surface chemical structure of the Ni/NiO/RGO, NiO, RGO and GO by the Fourier transform IR (FTIR). As shown in Fig. 2(a), –OH (3376 cm^{-1}), C=O (1732 cm^{-1}), and C=C (1624 cm^{-1}) functional groups in GO can be observed.[58] However, it is observed that the typical peaks of –OH (3376 cm^{-1}) and C=O (1732 cm^{-1}) have nearly disappeared in RGO (Fig. 2(b)), exhibiting that the conversion of GO into RGO. Then again, the characteristic peaks of GO were not observed in Ni/NiO/RGO and the spectrum of the Ni/NiO/RGO (Fig. 2(d)) was similar to that of bare NiO (Fig. 2(c)), implying that the GO can be also reduced to RGO by the thermal treatment in nitrogen. The FTIR result is in accordance with that of XRD analysis. Besides, as well known, the high temperature thermos-annealing can cause the expelling of both physisorbed and chemisorbed water molecules, thereby resulting in the disappearance of water in samples. Thus, in principle, hydroxide ions at 3470 cm^{-1} should not be observed on pure NiO and Ni/NiO/RGO after the thermal treatment at 400 °C. Nevertheless, the –OH peak is still observed in Fig. 2(c) and (d). The observed bands are due to the fact that the calcined nanoparticles tend to physically absorb the water during mixing and pelleting with KBr.

The surface morphology and structural properties of Ni/NiO/RGO hybrid and NiO are detected by SEM. As clearly seen from Fig. 3, when NiO nanoparticle were assembled onto RGO, its morphology pronouncedly evolved from the sheet-like architecture with the length of about 1.72 μm to a self-assembled hierarchical porous structure composed of the slackly packed Ni–NiO particulate with the homogeneous diameter of about 30 nm. This clearly suggests that the existence of RGO plays a paramount role in the crystallization process of Ni species during synthetic procedures. According to previous reports, this distinct NiO growth mechanism can be attributed to the strong synergic effect between Ni precursor and RGO. During the growth process, graphene, as the substrate, can conduct the NiO nanoparticle assembly growing by electrostatic adsorption in aqueous solution. Then the strong synergic effect can direct the nanoparticle oriented growth. The oriented attachment mechanism describes the spontaneous self-organization of adjacent particles, so that they share a common crystallographic orientation, followed by the joining of these particles at a planar interface. The process is specially connected with the nano-crystalline regime, where
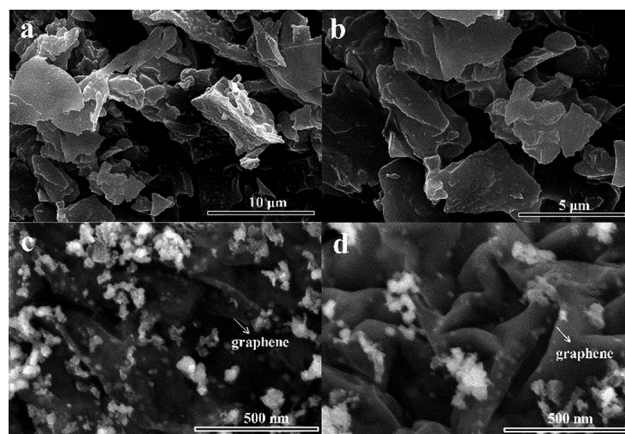

Fig. 2 FT-IR spectra of (a) GO, (b) RGO, (c) NiO and (d) Ni/NiO/RGO.

Fig. 3 SEM images of NiO (a and b) and Ni/NiO/RGO (c and d).

bonding between the particles reduces the overall energy by removing the surface energy associated with unsatisfied bonds.[59] As a result, the NiO nano-aggregates can be obviously downsized from sheet-like architecture for NiO to a self-assembled hierarchical porous structure for Ni/NiO/RGO hetero-structure. The results are also consistent with the TEM imaging in Fig. 4.

The microstructure of Ni/NiO/RGO hybrid is detected by TEM in Fig. 4. The selected area electron diffraction (SAED) pattern (Fig. 4(a) inset), clearly shows the features of both NiO and Ni, which is in accordance with the XRD analysis. The high-resolution TEM (HRTEM) image is shown in Fig. 4(b), which reveals the interplanar spacing of the hybrid. The lattice spacing of approximately 0.24 and 0.2 nm are ascribed to the (111) plane of NiO and the (111) plane of Ni, respectively. Importantly, the metallic Ni is located around and intimately contacted with the NiO nanoparticles. And a clear Ni–NiO interfaces can be identified, suggesting occurrence of the strong Ni–NiO interaction upon their assembly upon the RGO nanosheets. Overall, it can be unambiguously inferred from results above that the nickel metal oxides are actually a composite heterostructure of the strongly interfaced Ni^o–NiO complexes. Furthermore, from TEM images, no obvious aggregation of nanoparticles can be seen on the graphene sheets. Markedly, the folded structure of the graphene may not only restrain nanoparticles from accumulation and allow a good distribution on the graphene, but also may affect the morphology and size of the Ni/NiO/RGO hybrid and endow the hybrid more reactive sites. Moreover, the existence of a small quantity of Ni^o could significantly enhance the electrochemical activity of NiO and plays an important role in controlling the morphology of the nano-hybrid.[60] Since the being of the Ni^o, the obtained Ni^o–NiO complex exhibits remarkably enhanced electrochemical activity because of the unique hierarchical structure and possible better synergetic effect from the triple junctions.[61] Also, in this nano-heterostructure, the thin surface layer of NiO has high redox activity, while the Ni^o metallic particle on the NiO surface serves as the channel for the fast electron transport and a short diffusion path to the current collector, thereby enhancing the

pseudocapacitance.[55] At the same time, Ni–NiO complexes also act as spacers, which efficiently prevent the restacking of the graphene sheets, avoiding the loss of the active surface area, furnishing better access for the electrolyte into the entire graphene structure. The characteristic of synergistic effect between the Ni–NiO complexes and graphene raises the effective electrolyte-electrode interfacial area, giving a fast direction for the transport of electrolyte ions to facilitate electrolyte diffusion and intercalation, and consequently facilitates the Faraday reaction. As a result, the Ni/NiO/RGO hybrid has an advantage in its electrochemical high-performance.

The specific surface area and porosity distribution characteristics of the hybrid were further explored by the N$_2$ adsorption/desorption isotherms in Fig. 5. The porous structure of Ni/NiO/RGO hybrid can be demonstrated by the hysteresis loops in Fig. 5(c). The curve in Fig. 5(d) displays a narrow pore-size distribution at 1.76 nm and a broad pore-size distribution around 12.52 nm, implying that the hybrid essentially contains mesoporous with a minor fraction of microporous structure. The hybrid shows a specific surface area of 55.10 m^2 g^{-1} and an average pore size of 10.25 nm. Nevertheless, the specific surface area and the average pore size of NiO are 42.05 m^2 g^{-1} and 15.67 nm, respectively, exhibiting that the Ni/NiO/RGO hybrid shows a bigger surface area and better uniform pore size distribution, which is consistent with the SEM and TEM analysis results. That is valuable for the supercapacitor applications to work for a high performance electrode.

The electrochemical performances of Ni/NiO/RGO hybrid as electrode materials for supercapacitors were evaluated by cyclic voltammetry (CV), chronopotentiometry and electrochemical impedance spectroscopy (EIS).

Fig. 6 shows the CV curves of Ni/NiO/RGO hybrid and bare NiO at a scan rate of 10 mV s^{-1}. It can be seen that each CV curve exhibits a pair of strong redox peaks, indicating that the capacitance characteristic is mainly governed by pseudocapacitor
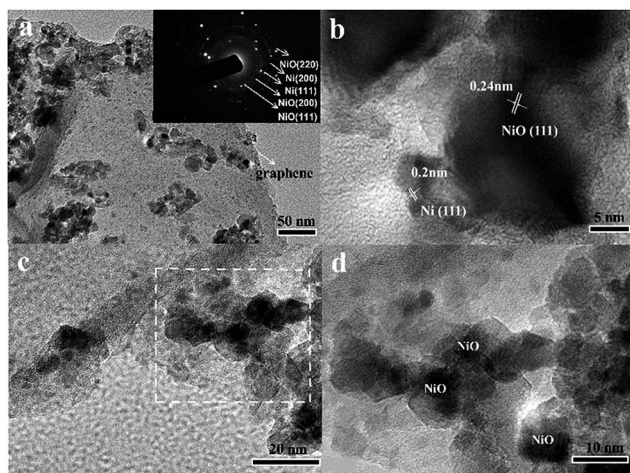

Fig. 4   TEM image (a and c) (the inset image is the SAED pattern of Ni/NiO/RGO) and HRTEM (b and d) of Ni/NiO/RGO hybrid.
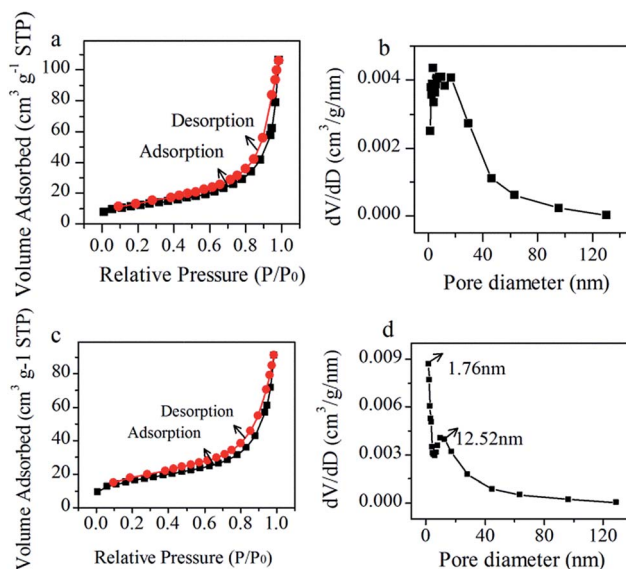

Fig. 5   N$_2$ adsorption/desorption isotherms and pore size distribution curve of NiO (a and b) and Ni/NiO/RGO hybrid (c and d).
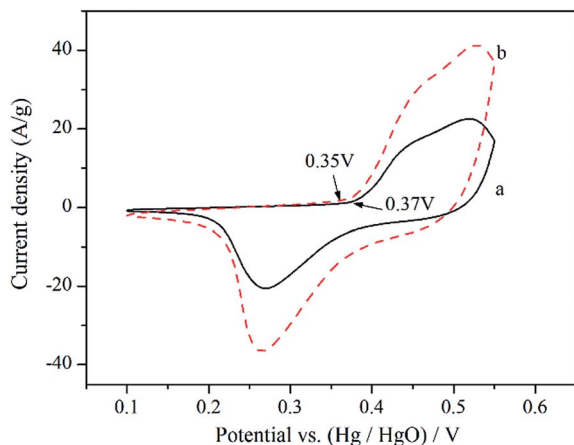
Fig. 6 CV curves of (a) NiO and (b) Ni/NiO/RGO hybrid at a scan rate of 10 mV s^{-1}.

Fig. 8 Chronopotentiometry curves of Ni/NiO/RGO (a) and NiO (b) at various current densities of 2, 3, 4, 5, 10, 15 and 20 A g^{-1}, (c) specific capacitances at various discharge current densities for NiO and Ni/NiO/RGO hybrid, (d) cycling performance of NiO and Ni/NiO/RGO hybrid at a current density of 5 A g^{-1}.

behavior based on a fast redox process according to the following equation: $NiO + OH^- \leftrightarrow NiOOH + e^-$.[62,63] It is also generally accepted that the area covered by the CV curves can be used to estimate the capacitance of a material.[54] As can be seen easily, the area under the CV curves for Ni/NiO/RGO hybrid is much larger than that of bare NiO, demonstrating the higher specific capacitance.

Furthermore, it is observed that the onset potential of the oxidation peak of the Ni/NiO/RGO hybrid (0.35 V) shifts in the negative direction compared to that of the pristine NiO (0.37 V). The shift of the onset potential of oxidation peak exhibits that a decreased energy barrier would be required for the NiO → NiOOH reaction, which indicates the improvement in the reaction kinetics and the better electrochemical activities of the NiO.[46]

Fig. 7 shows the CV curves of the Ni/NiO/RGO at scan rates ranging from 1 to 10 mV s^{-1}. Obviously, the symmetry of the CV curves is significantly distorted as the scan rate increases, which is caused by the kinetic irreversibility of the redox process.[64] In addition, as the scan rate increases, the oxidation peak shifts in
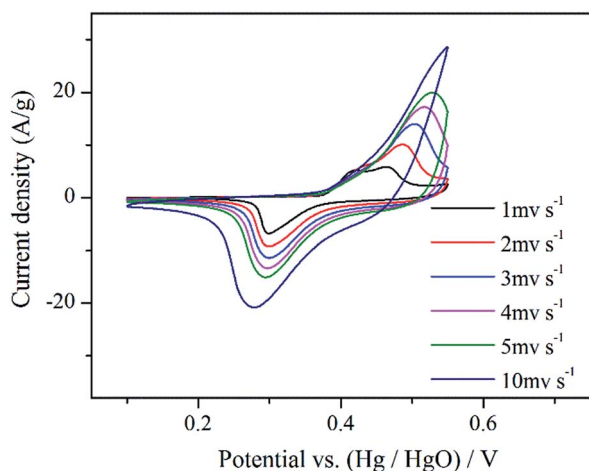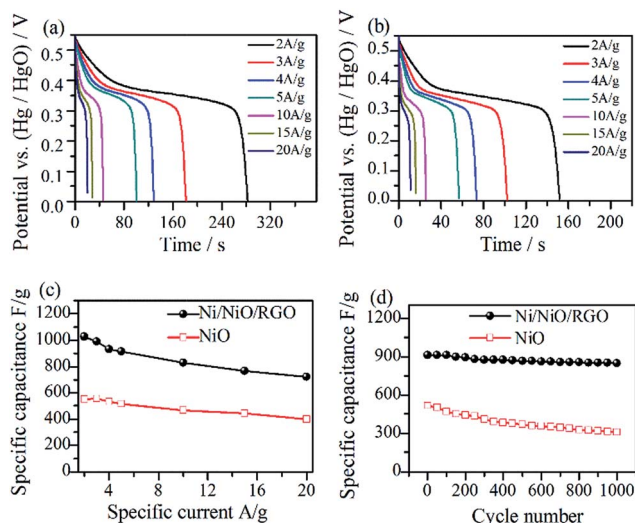
the more positive directions and the reduction peak shifts in the more negative directions, which is mainly due to the limitation of the ion diffusion rate to satisfy electronic neutralization during the redox reaction.[65]

To further calculate the specific capacitance and comprehend the rate capability of Ni/NiO/RGO hybrid electrode, the chronopotentiometry measurements were carried out at various current densities and the results are shown in Fig. 8.

The specific capacitances of the hybrid electrode are calculated from the discharge time and the results are plotted in Fig. 8(c). The Ni/NiO/RGO hybrid exhibits specific capacitances of 1027.27, 989.45, 934.55, 912.73, 830.91, 766.36 and 720 F g^{-1} at 2, 3, 4, 5, 10, 15 and 20 A g^{-1}, respectively, which are much higher than those achieved from the bare NiO (551.64, 558, 533.82, 516.36, 467.27, 441.82, and 400 F g^{-1}, respectively). Moreover, even at a very high current density of 20 A g^{-1}, nearly 70% of initial capacitance value remains, exhibiting the unusual rate capability of the Ni/NiO/RGO hybrid electrode. Notably, the specific capacitance gradually decreased with the increase of current densities, which could be due to the resistance of Ni/NiO/RGO hybrid and the deficient faradic redox reaction at a higher current density.[66] In addition, the fantabulous cycle stability of the Ni/NiO/RGO hybrid and pure NiO electrode at a current density of 5 A g^{-1} is investigated (Fig. 8(d)). After uninterrupted 1000 cycles, the specific capacitance value can be still stabilized at 92.95% of that of the initial specific capacitance for Ni/NiO/RGO, but, sharply declines by 60.07% for bare NiO after 1000 cycles. The results exhibit the excellent electrochemical stability of the Ni/NiO/RGO hybrid electrode for pseudocapacitors.

Fig. 9 displays the Nyquist plots of the Ni/NiO/RGO hybrid and the NiO electrodes, which were measured from 100 KHz to 0.1 Hz. All the curves are composed of a semicircle at high-frequency followed by a line at the low-frequency. The

Fig. 7 CV curves of Ni/NiO/RGO at scan rates of 1 mV s^{-1}, 2 mV s^{-1}, 3 mV s^{-1}, 4 mV s^{-1}, 5 mV s^{-1} and 10 mV s^{-1} in 6 M KOH.
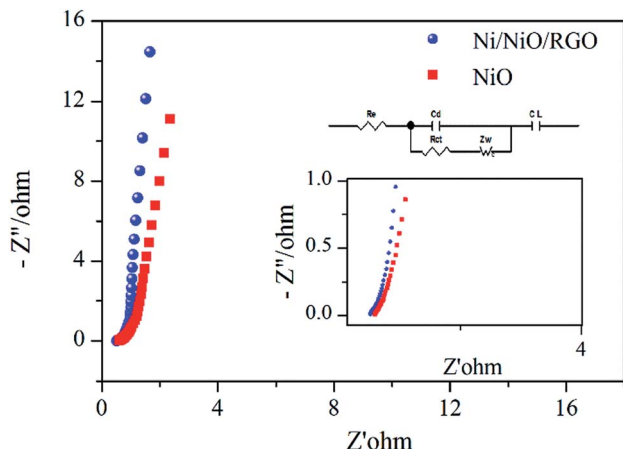
Fig. 9 Nyquist plots of the Ni/NiO/RGO and NiO electrical, the insert are the partially enlarged view of Nyquist and the equivalent electrical circuit mode plot.

Table 1 Parameters fitted from EIS spectra

Sample	R_e (Ω)	R_{ct} (Ω)	Z_w
NiO	0.7069	0.1062	0.7477
Ni/NiO/RGO	0.6259	0.09958	0.4788

resistance (R_e) in the equivalent circuit (see inset in Fig. 9), which includes the combinational resistances of the electrolyte resistance, intrinsic resistance of active materials and contact resistance at the active material/current collector interface, can be earned by the intercept with the real axis at high frequency.

The semicircle is connected with the charge transfer resistance (R_{ct}).[67,68] According to the fitting, the calculated R_e and R_{ct} of the electrodes are demonstrated in Table 1. Apparently, the Ni/NiO/RGO hybrid electrode displays lower R_e and R_{ct} than NiO electrode due to the higher electron conductivity ability of the hybrid. Moreover, a smaller R_{ct} means a smaller charge-transfer resistance. Additionally, the Z_w, which expresses the Warburg impedance, is related to ion diffusion and transfer between electrode and electrolyte. A smaller Z_w indicates a greater ion-diffusion-transfer rate. Lower resistance and greater ion-diffusion-transfer rate for Ni/NiO/graphene hybrid signify a faster charge-transfer process. Obviously, the distinct electrochemical behavior of the Ni/NiO/graphene can be exclusively as result of its unique hierarchical porous heterostructure. Taken together, consistent with the CV and chronopotentiometry results, the results also indicate that the Ni/NiO/RGO hybrid possesses a good current rate property.

Conclusions

Given that the superior electrochemical high-performance of the self-assembled hierarchical porous structure of Ni/NiO/RGO nano-hybrid largely counts on its surface microstructure and electronic conductivity, we propose three factors. Ahead, the hybrid shows a larger specific surface area and an a smaller

average pore size, so the inner more active sites of the electrode-material can be fully to effectively interact with electrolytes. Second, compared with the sheet-like NiO, the self-assembled hierarchical hybrid exhibits the uniform and unagglomerate nanoparticles, which can keep the effective contact areas of active electrode-materials and electrolyte sufficiently. Third, due to the characteristic of strong synergistic effect between the Ni–NiO complexes and graphene, the exposed NiO–Ni nano-interfaces may be synergistically active sites for the Faraday reaction, which can greatly improve electronic conductivity and give a fast direction for the transport of electrolyte ions. Finally, these factors are anticipated to furnish the intrinsical level of capacitive performance for supercapacitors.

In summary, self-assembled hierarchical porous structure of Ni/NiO/RGO hybrid, an encouraging and fantabulous electrode material for supercapacitors, was synthesized through a facile sol–gel process method combined with subsequent *in situ* treatment at 400 °C. When used as the electrode material, it displays a high specific capacitance, unusual rate capability and good cycle stability. The high specific capacitance is 1027.27 F g^{-1} at a current density of 2 A g^{-1} and 720 F g^{-1} at 20 A g^{-1}.

The feature of synergistic effect between the Ni–NiO complexes and graphene builds the effective electrode-electrolyte interfacial area, giving a fast direction for the transport of electrolyte ions, which can facilitate the Faraday reaction. Finally, we believe that the superior electrochemical performance, cost effective, and easy fabrication of the Ni/NiO/RGO hybrid electrode materials would have a promising application in electrochemical energy storage.

Notes and references

1 C. M. Winter and R. J. Brodd, *Chem. Rev.*, 2004, **104**, 4245.
2 J. Li, Y. Wang, J. Tang, Y. Wang, T. Wang, L. Zhang and G. Zheng, *J. Mater. Chem. A*, 2015, **3**, 2876.
3 W. Liu, C. Lu, X. Wang, K. Liang and B. K. Tay, *J. Mater. Chem. A*, 2015, **3**, 624.
4 H. Chen, J. Jiang, Y. Zhao, L. Zhang, D. Guo and D. Xia, *J. Mater. Chem. A*, 2015, **3**, 428.
5 N. Mahmood, C. Zhang, H. Yin and Y. Hou, *J. Mater. Chem. A*, 2014, **2**, 15.
6 T. Chen and L. Dai, *J. Mater. Chem. A*, 2014, **2**, 10756.
7 Y. Bai, W. Wang, R. Wang, J. Sun and L. Gao, *J. Mater. Chem. A*, 2015, **3**, 12530.
8 H. Wang, H. Yi, X. Chen and X. Wang, *J. Mater. Chem. A*, 2014, **2**, 1165.
9 Y. J. He, J. F. Peng, W. Chu, Y. Z. Li and D. G. Tong, *J. Mater. Chem. A*, 2014, **2**, 1721.
10 J. R. Miller and P. Simon, *Science*, 2008, **321**, 651.

11 P. S. Simon and Y. Gogotsi, *Nat. Mater.*, 2008, **7**, 845.

12 X. Peng, L. L. Peng, C. Z. Wu and Y. Xie, *Chem. Soc. Rev.*, 2014, **43**, 3303.

13 L. An, K. Xu, W. Li, Q. Liu, B. Li, R. Zou, Z. Chen and J. Hu, *J. Mater. Chem. A*, 2014, **2**, 12799.

14 S. Sun, J. Lang, R. Wang, L. Kong, X. Li and X. Yan, *J. Mater. Chem. A*, 2014, **2**, 14550.

15 Y. Li, L. Cao, L. Qiao, M. Zhou, Y. Yang, P. Xiao and Y. Zhang, *J. Mater. Chem. A*, 2014, **2**, 6540.

16 S. Min, C. Zhao, Z. Zhang, G. Chen, X. Qian and Z. Guo, *J. Mater. Chem. A*, 2015, **3**, 3641.

17 K. Xu, W. Li, Q. Liu, B. Li, X. Liu, L. An, Z. Chen, R. Zou and J. Hu, *J. Mater. Chem. A*, 2014, **2**, 4795.

18 J. T. Zhang, S. Liu, G. L. Pan, G. R. Li and X. P. Gao, *J. Mater. Chem. A*, 2014, **2**, 1524.

19 Z. Li, J. Han, L. Fan, M. Wang, S. Tao and R. Guo, *Chem. Commun.*, 2015, **51**, 3053.

20 S. Chen, W. Xing, J. Duan, X. Hu and S. Z. Qiao, *J. Mater. Chem. A*, 2013, **1**, 2941.

21 L. L. Z. K. Zhang, H. S. O. Chan, X. S. Zhao and J. S. Wu, *J. Mater. Chem. A*, 2011, **21**, 7302.

22 S. P. M. D. Stoller, Y. Zhu, J. An and R. S. Ruoff, *Nano Lett.*, 2008, **8**, 3498.

23 X. Lang, A. Hirata, T. Fujita and M. Chen, *Nat. Nanotechnol.*, 2011, **6**, 232.

24 K. Zhang, L. L. Zhang, X. S. Zhao and J. S. Wu, *J. Mater. Chem. A*, 2011, **21**, 2663.

25 R. B. Rakhi, W. Chen, D. Cha and H. N. Alshareef, *Nano Lett.*, 2012, **12**, 2559.

26 J. Yang, C. Yu, X. Fan, Z. Ling, J. Qiu and Y. Gogotsi, *J. Mater. Chem. A*, 2013, **1**, 1963.

27 M. S. Kolathodi, M. Palei and T. S. Natarajan, *J. Mater. Chem. A*, 2015, **3**, 7513.

28 Y. Wang, S. Gai, N. Niu, F. He and P. Yang, *J. Mater. Chem. A*, 2013, **1**, 9083.

29 J. Zhang and X. S. Zhao, *J. Phys. Chem. C*, 2012, **116**, 5420.

30 J. Zhang, J. Jiang, H. Li and X. S. Zhao, *Energy Environ. Sci.*, 2011, **4**, 4009.

31 A. K. Geim and K. S. Novoselov, *Nat. Mater.*, 2007, **6**, 183.

32 D. A. Dikin, S. Stankovich, E. J. Zimney, R. D. Piner, G. H. Dommett, G. Evmenenko, S. T. Nguyen and R. S. Ruoff, *Nature*, 2007, **448**, 457.

33 V. Singh, D. Joung, L. Zhai, S. Das, S. I. Khondaker and S. Seal, *Prog. Mater. Sci.*, 2011, **56**, 1178–1271.

34 C. Long, L. Jiang, T. Wei, J. Yan and Z. Fan, *J. Mater. Chem. A*, 2014, **2**, 16678.

35 Y. B. Tan and J.-M. Lee, *J. Mater. Chem. A*, 2013, **1**, 14814.

36 C. Xu, B. Xu, Y. Gu, Z. Xiong, J. Sun and X. S. Zhao, *Energy Environ. Sci.*, 2013, **6**, 1388.

37 Y. Wang, Y. P. Wu, Y. Huang, F. Zhang, X. Yang, Y. F. Ma and Y. S. Chen, *J. Phys. Chem. C*, 2011, **115**, 23192.

38 Y. Liu, Y. Ma, S. Guang, H. Xu and X. Su, *J. Mater. Chem. A*, 2014, **2**, 813.

39 Z. Zhang, K. Chi, F. Xiao and S. Wang, *J. Mater. Chem. A*, 2015, **3**, 12828.

40 X. Cao, Y. Shi, W. Shi, G. Lu, X. Huang, Q. Yan, Q. Zhang and H. Zhang, *Small*, 2011, **7**, 3163.

41 L. Jiang, R. Zou, W. Li, J. Sun, X. Hu, Y. Xue, G. He and J. Hu, *J. Mater. Chem. A*, 2013, **1**, 478.

42 U. M. Patil, M. S. Nam, J. S. Sohn, S. B. Kulkarni, R. Shin, S. Kang, S. Lee, J. H. Kim and S. C. Jun, *J. Mater. Chem. A*, 2014, **2**, 19075–19083.

43 S. Wu, W. Chen and L. Yan, *J. Mater. Chem. A*, 2014, **2**, 2765.

44 F. Yang, J. Yao, F. Liu, H. He, M. Zhou, P. Xiao and Y. Zhang, *J. Mater. Chem. A*, 2013, **1**, 594.

45 S. Yang, X. Song, P. Zhang and L. Gao, *J. Mater. Chem. A*, 2013, **1**, 14162.

46 M. L. Huang, C. D. Gu, X. Ge, X. L. Wang and J. P. Tu, *J. Power Sources*, 2014, **259**, 98.

47 A. H. H. F. Jiao, A. Harrison, A. Berko, A. V. Chadwick and P. G. Bruce, *J. Am. Chem. Soc.*, 2008, **130**, 5362.

48 G. F. Cai, J. P. Tu, J. Zhang, Y. J. Mai, Y. Lu, C. D. Gu and X. L. Wang, *Nanoscale*, 2012, **4**, 5724.

49 Y. Bai, M. Du, J. Chang, J. Sun and L. Gao, *J. Mater. Chem. A*, 2014, **2**, 3834.

50 Y. Chen, Z. Huang, H. Zhang, Y. Chen, Z. Cheng, Y. Zhong, Y. Ye and X. Lei, *Int. J. Hydrogen Energy*, 2014, **39**, 16171.

51 C. Wu, Q. Shen, R. Mi, S. Deng, Y. Shu, H. Wang, J. Liu and H. Yan, *J. Mater. Chem. A*, 2014, **2**, 15987.

52 H. Wang, H. Yi, X. Chen and X. Wang, *J. Mater. Chem. A*, 2014, **2**, 3223.

53 P. Cao, L. Wang, Y. Xu, Y. Fu and X. Ma, *Electrochim. Acta*, 2015, **157**, 359.

54 X. J. Zhu, H. L. Dai, J. Hu, L. Ding and L. Jiang, *J. Power Sources*, 2012, **203**, 243.

55 A. K. Singh, D. Sarkar, G. G. Khan and K. Mandala, *J. Mater. Chem. A*, 2013, **1**, 12759.

56 W. S. Hummers and R. E. Offeman, *J. Am. Chem. Soc.*, 1958, **80**, 1339.

57 P. S. Patil and L. D. Kadam, *Appl. Surf. Sci.*, 2002, **199**, 211.

58 D. C. Marcano, D. V. Kosynkin, J. M. Berlin, A. Sinitskii, Z. Z. Sun, A. Slesarev, L. B. Slemany, W. Lu and J. M. Tour, *ACS Nano*, 2010, **4**, 4806.

59 L. Q. Mai, F. Yang, Y. L. Zhao, X. Xu, L. Xu and Y. Z. Luo, *Nat. Commun.*, 2011, **2**, 381.

60 F. F. Yuan, Y. H. Ni, L. Zhang, S. M. Yuan and J. D. Wei, *J. Mater. Chem. A*, 2013, **1**, 8438.

61 M. Gong, W. Zhou, M. Tsai, J. G. Zhou, M. Y. Guan, M. Lin, B. Zhang, Y. F. Hu, D. Wang, J. Yang, S. J. Pennycook, B. Hwang and H. J. Dai, *Nat. Commun.*, 2014, **5**, 4695.

62 K. C. Liu and M. A. Anderson, *J. Electrochem. Soc.*, 1996, **143**, 124.

63 C. Natarajan, H. Matsumoto and G. Nogami, *J. Electrochem. Soc.*, 1997, **144**, 121.

64 Y. Z. Su, K. Xiao, N. Li, Z. Q. Liu and S. Z. Qiao, *J. Mater. Chem. A*, 2014, **2**, 13845.

65 J. W. Lee, T. Ahn, D. Soundararajan, J. M. Ko and J. D. Kim, *Chem. Commun.*, 2011, **47**, 6305.

66 Z. Lu, Z. Chang, W. Zhu and X. Sun, *Chem. Commun.*, 2011, **47**, 9651.

67 A. D. Jagadale, V. S. Kumbhar, D. S. Dhawale and C. D. Lokhande, *Electrochim. Acta*, 2013, **98**, 32.

68 J. Gamby, P. L. Taberba, P. Simon, J. F. Fauvarque and M. Chesneau, *J. Power Sources*, 2001, **101**, 109.